STRUCTURAL OPTIMIZATION AND RECENT LARGE GROUND ANTENNA INSTALLATIONS*

Roy Levy
Jet Propulsion Laboratory
California Institute of Technology
Pasadena, California

*The research described in this paper was carried out by the Jet Propulsion Laboratory, California Institute of Technology, under a contract with the National Aeronautics and Space Administration.

* C-5

NASA 70-METER ANTENNA CONSTRUCTION

Within the past several years, the Jet Propulsion Laboratory has designed and built major ground antenna structures in Spain, Australia, and California. One of the antennas at each location is a 70-meter-diameter structure that is a retrofit of the existing 64-meter antenna. The 64-meter existing antennas were first stripped back to a 34-meter interior and then completely new construction with deeper trusses was added to extend the interior to 70 meters. The 70-meter project included the rare opportunity to collect field data to compare with predictions of the finite-element analytical models. The new quadripod design was tested for its lower mode natural frequencies and the main reflector was measured by theodolite to determine deflections of subsets of the backup-structure deformations under load. The emphasis here will be to examine measurement results and possibly provide some appreciation of the relationship of predictions made from the design model to actual measurements.

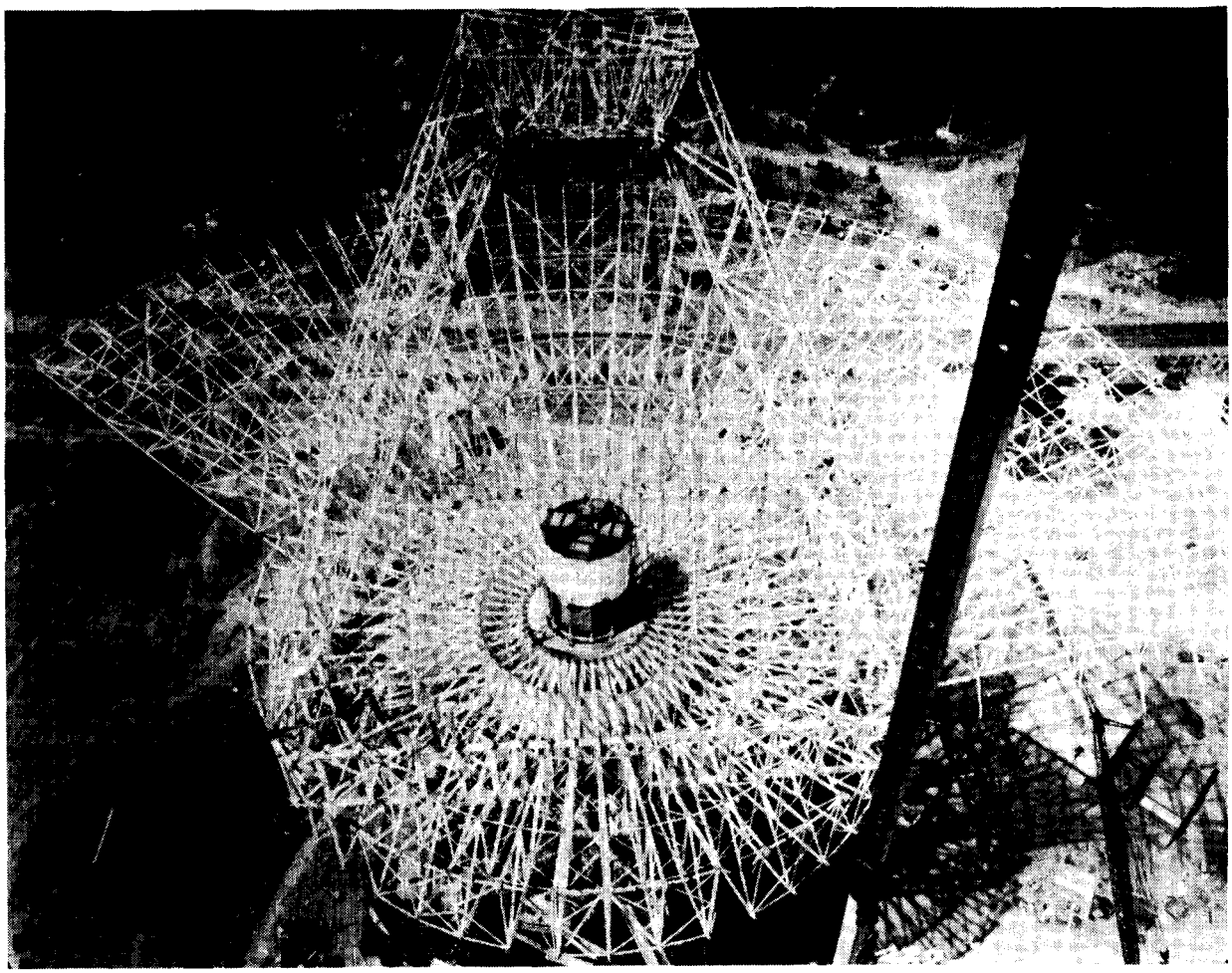

70-METER COMPLETED ANTENNA

All the 70-meter antennas are steerable both in elevation and azimuth and are characterized by extremely precise surface accuracy and boresight pointing error requirements. These requirements must be maintained for a spectrum of environmental wind and variable-attitude gravity loading. As an example of the required precision, the root-mean-square surface error (after a least-square fit (ref. 1) to an alternative rigid-body-shifted ideal surface) is only 20 to 50 millinches (mils). Furthermore, before any least-squares fitting, the maximum deflection at the 115-foot radius for the 70-meter antenna changes by only about 1.5 inches over the elevation angle range. The structure's contribution to the microwave beam pointing error should be only a few millidegrees, and this includes a penalty due to the rigid-body rotation of the best fitting surface.

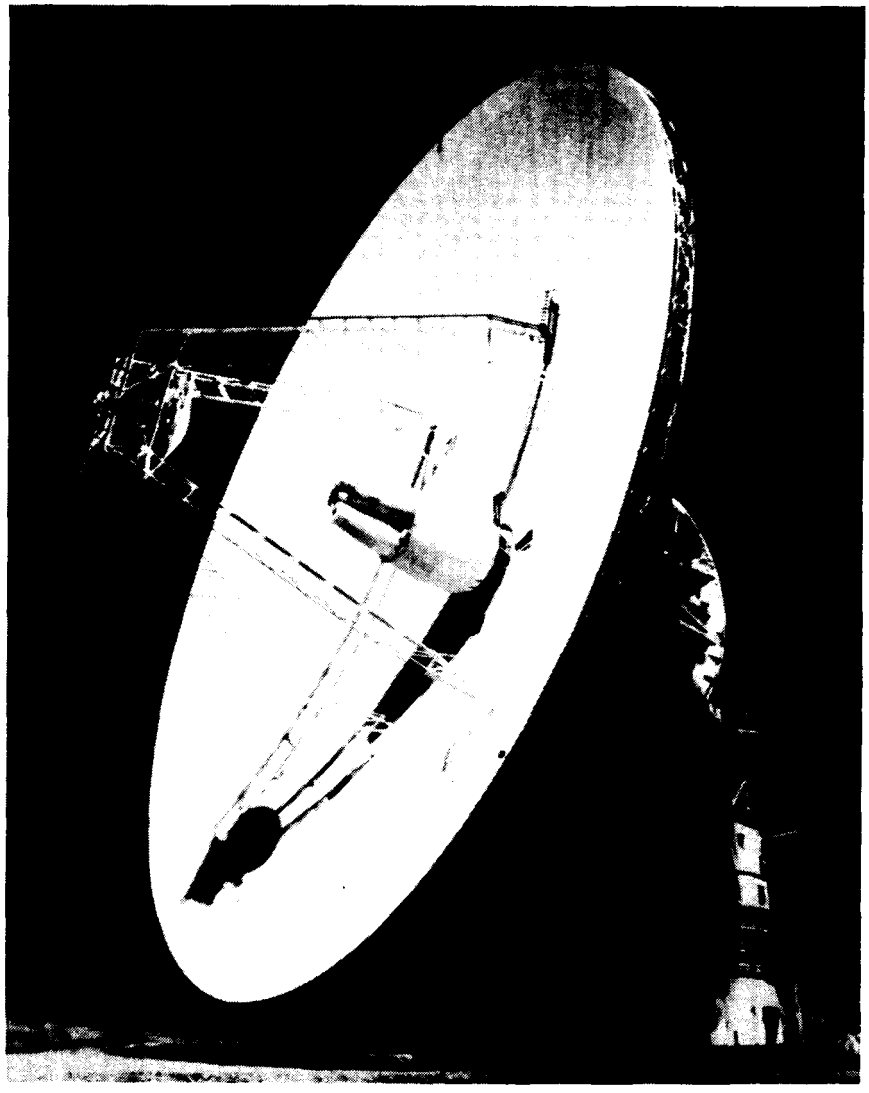

ANTENNA OPTIMIZATION SOFTWARE

The diverse requirements of maintaining both the surface shape and the pointing accuracy constraints are in conflict when it comes to the design. Because of this, intuitive trial-and-error design and analysis procedures are both time consuming and likely to be unproductive. About 15 years ago, we began the development of our own special-purpose analysis and automated antenna-design-optimization software, called the "JPL-IDEAS" (Iterative Design of Antenna Structures) program. At the first public description (ref. 2) of the program, we were chagrined to learn that Grumman Aerospace had predated us in the use of the name "IDEAS" so that we immediately tacked on the "JPL-" prefix. Since then, there has been a proliferation of computer programs with this name, but the ambiguity does not yet seem to have caused confusion.

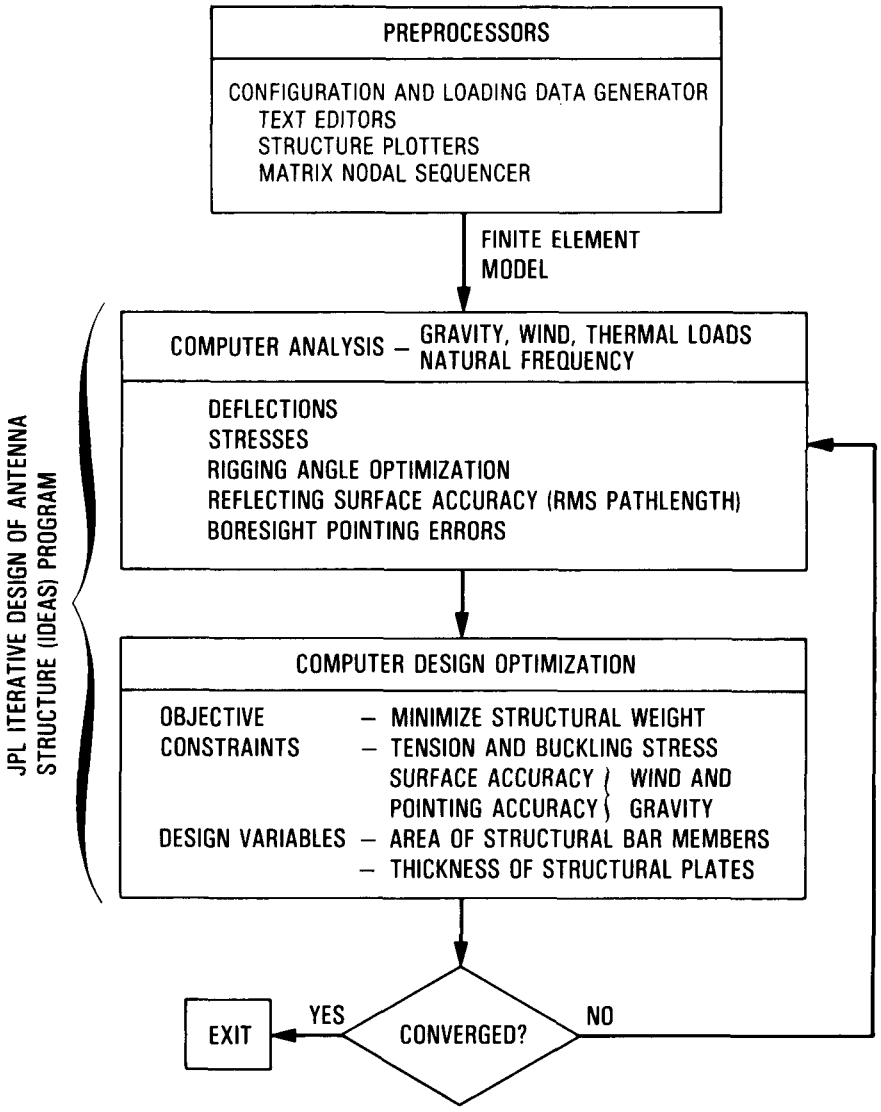

ANTENNA STRUCTURAL DESIGN CONSTRAINTS

The compliance-type microwave performance requirements of maintaining a nearly ideal microwave reflecting surface figure and providing accurate pointing of the electronic beam lead to a specialized structural optimization formulation. The way we establish virtual ("dummy") loading vectors that allow us to derive the gradients of the compliance constraints and the procedures for applying optimality criteria, and finding the Lagrange multipliers has appeared in refs. 2 through 6. For convenient reference here, the figures below illustrate the nature of the structural deformations and geometric relationships involved in the surface path-length and pointing-error constraints.

PRIMARY COMPLIANCE CONSTRAINTS

- **MICROWAVE PATH-LENGTH-ERROR CONSTRAINT**
  - **MAXIMUM PERMISSIBLE ROOT-MEAN-SQUARE PATH-LENGTH ERROR FROM A BEST-FITTING ALTERNATE SURFACE**

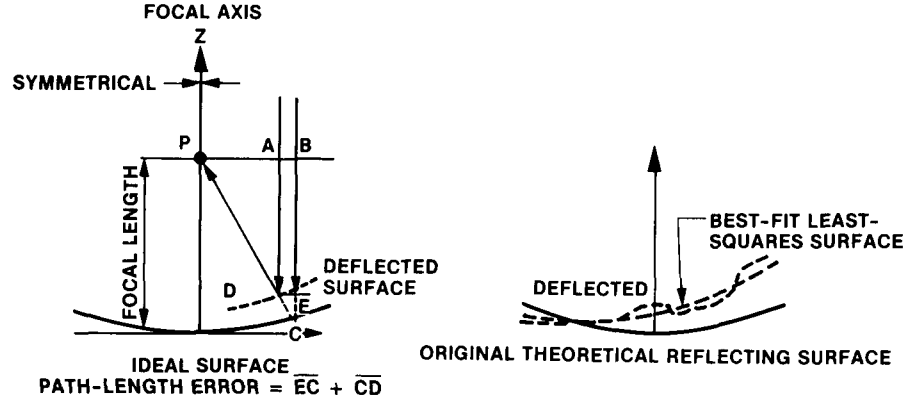

- **BORESIGHT POINTING-ERROR CONSTRAINT**

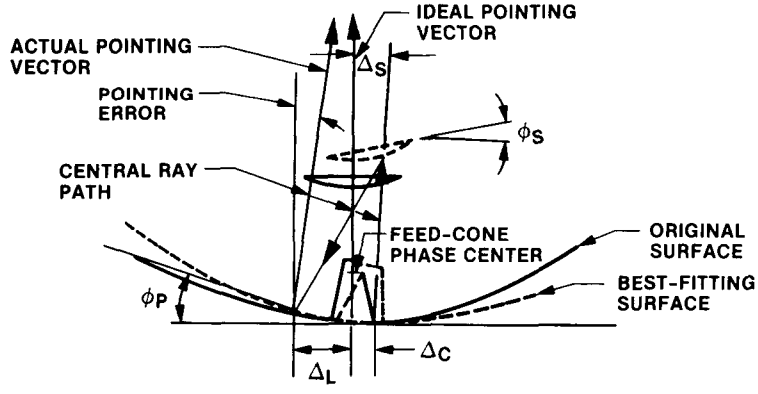

FIVE COMPONENTS OF ANTENNA POINTING ERROR

- Δ_L - BEST-FIT PARABOLOID LATERAL VERTEX SHIFT
- ϕ_P - BEST-FIT PARABOLOID AXIS ROTATION
- Δ_S - SUBREFLECTOR LATERAL TRANSLATION
- Δ_C - FEED-CONE LATERAL TRANSLATION
- ϕ_S - SUBREFLECTOR ROTATION

DESIGN FOR MINIMUM NATURAL FREQUENCY

In addition to the antenna microwave performance constraints, there are requirements to maintain minimum natural frequencies in conjunction with control system instability. We found that the minimum natural frequency of the 70-meter structure was, for a decoupled quadripod mode, similar to that of the quadripod supported independently on a rigid foundation. This permitted a simplified design of the quadripod for minimum natural frequency: the quadripod was considered an isolated, stand-alone component. An algorithm to obtain maximum natural frequency for a prespecified structural mass was described in ref. 7 and executed with no difficulty. In the same reference and in others (refs. 8 and 9), it was found necessary to scale the design when the optimization was formed in the traditional way of minimizing the structural mass for a specified constraint on minimum natural frequency. Since then, the scaling requirement has been removed from our algorithm. We show the highlights of our more recent algorithm in the figure. With this formulation, the natural-frequency design case can be handled as another constraint case along with compliance and stress constraints in conventional optimality criteria problem formulations.

RAYLEIGH QUOTIENT, $\omega^2 = \frac{\phi^T K \phi}{\phi^T M \phi}$

$\frac{\partial \omega^2}{\partial a_i}$ LEADS TO: $\frac{1}{\underline{M}\, a_i} \times V_i$

WHERE $V_i = \phi^T k_i \phi - \omega^2 \phi^T m_i \phi$

NOMENCLATURE

- K = STIFFNES MATRIX
- M = MASS MATRIX
- ω^2 = EIGENVALUE
- ϕ = EIGENVECTOR
- $\underline{M} = \phi^T M_i \phi$
- a_i = DESIGN VARIABLE
- k_i, m_i = ASSOCIATED WITH a_i
- $\underline{M} = M_F + M_s$ WHERE M_F DOES NOT DEPEND ON a_i AND M_s DOES
- L_i, E_i, γ_i = LENGTH, MODULUS, DENSITY ASSOCIATED WITH a_i
- c_R, c_D = ELEMENT STRESS RESULTANTS FOR EIGENVECTOR

	DISPLACEMENT METHOD	FORCE METHOD
VIRTUAL WORK	$\phi^T K \phi$	$C_R\, C_D\, L/AE$

THEN $V_i = (L/aE)_i\, (c_R\, c_D')_i$, IN WHICH $C_D' = c_{R_i} - \omega^2 \phi^T m_i \phi\ (a/L\, C_R)_i$

LET $F_{IJ} = \frac{C_R\, C_D'}{\underline{M}\, E}$, THEN $\frac{\partial \omega^2}{\partial a_i} = F_{IJ}\, (L/a^2)_i$

FORM THE CONSTRAINT: $g_J = \omega_J^{*2} - \omega^2 \leqslant 0$, WHERE ω_J^* = PRESPECIFIED MINIMUM

THEN THE STANDARD OPTIMALITY CRITERION METHOD GIVES: $a_i' = (\sum_J (F_{IJ}/\gamma)_i\, \lambda_J)^{1/2}$

IN THE SPECIAL CASE OF ONE FREQUENCY CONSTRAINT,

$\lambda^{1/2} = [\omega^{*2} - \omega^2\, M_s/M - (\sum Va'/a)_{BOUNDED}]/(\sum F_{IJ}\, L\, (F_{IJ}/\gamma)^{1/2}/a^2$

OPTIMIZATION MODEL STATISTICS

The data show the relative complexity of the design-optimization problems. Both tabulations are for half-structure models with respect to one plane of symmetry. Most of our loadings are symmetrical with respect to this plane, but for design of the reflector for side wind loads, the design is automated for reflective symmetry and uses two different sets of boundary restraints. For the quadripod, we know that the lowest mode will be torsion with respect to its long axis; therefore, we design the quadripod for natural frequency with antisymmetric restraints at the plane of symmetry. On our UNISYS 1100/91 mainframe computer, a quadripod design is considered to be a small problem. However, the full 70-meter model design process is formidable. From 5 to 10 design cycles with about 10 to 15 path-length and pointing-error constraints could involve several hours of throughput and from $200 to $1000 in computer charges. The computer use is dominated by the analysis effort, which is dominated by decomposition of the stiffness matrix. Stress and Euler buckling constraints present no difficulties and these are handled as side constraints and readily treated by computing appropriate lower size bounds at each design cycle.

	HALF-STRUCTURE MODELS	
ITEM	QUADRIPOD	BACKUP STRUCTURE WITH QUADRIPOD
NODES	156	1986
UNCONSTRAINED DEGREES OF FREEDOM	420	5350
MAXIMUM NODAL WAVEFRONT	22	86
ROOT-MEAN-SQUARE NODAL WAVEFRONT	16	65
UNIVAC DECOMPOSITION TIME CPU, s	8	160
ROD ELEMENTS	443	6486
PLATES (TRIANGLE, SHEAR, QUADRILATERAL)	30	240
DESIGN VARIABLE GROUPS	42	708
UNEXCLUDED DESIGN VARIABLE GROUPS	39	435
WEIGHT OF STRUCTURE, kips	27	1235
PARASITIC WEIGHT, kips	11	635

IN-PLANT QUADRIPOD ASSEMBLY

The quadripod with its apex structure and a concrete weight to simulate the 12,000-pound subreflector were assembled at the fabricator's plant in Coslada, Spain, for a natural-frequency test. The apex structure is about 85 feet above the foundation. Each leg is a four-post, trapezoidal cross-section tower. The posts are 5-inch by 3-inch rectangular tubes. The struts and diagonals are smaller square tubes. The two deep side faces and the widest end face are Pratt-Howe trusses, and the narrowest end faces are solid plates. Outrigger braces connected to the second lowest bay of the tower truss can be seen near the bottom.

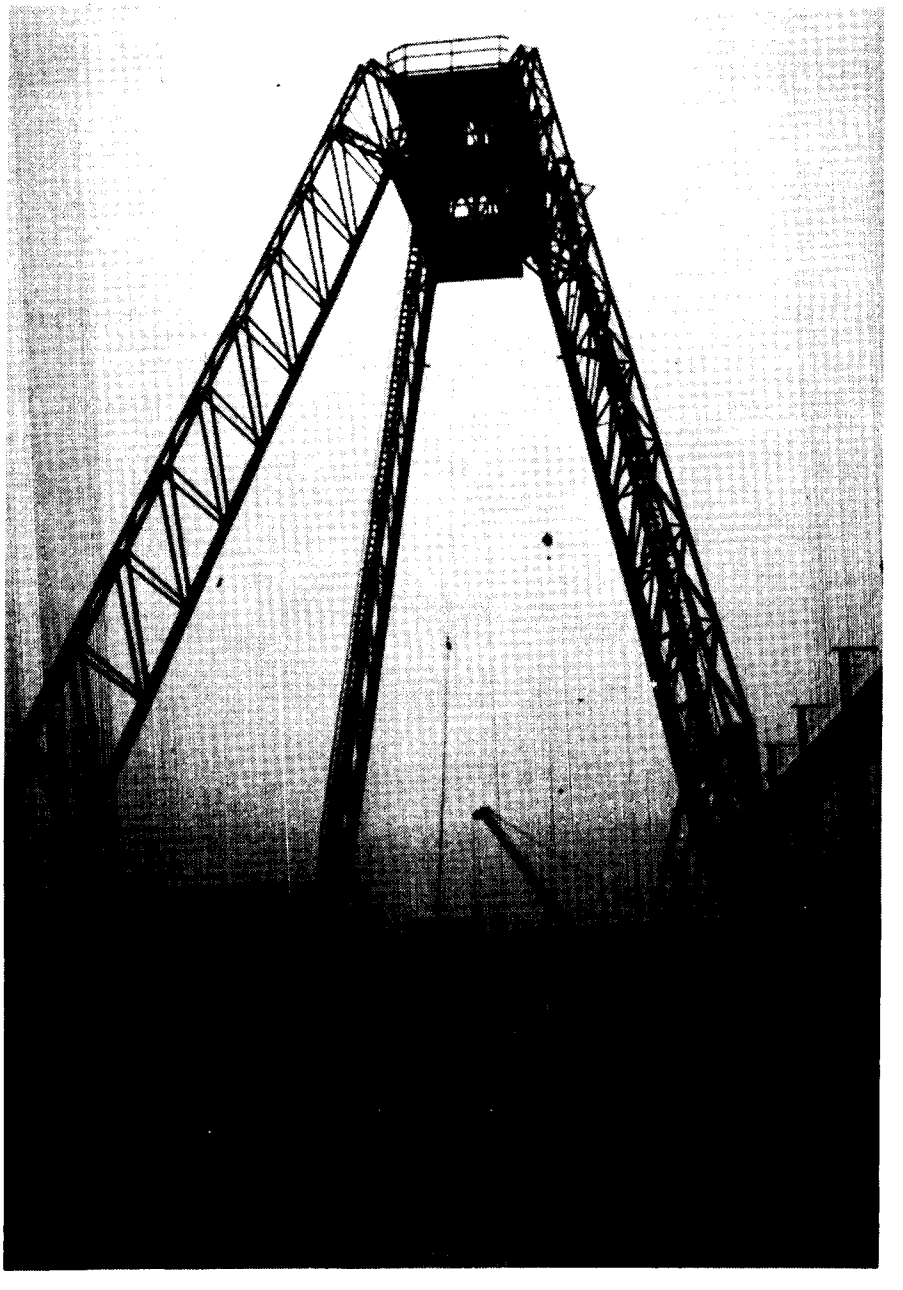

OUTRIGGER BRACE CONNECTION

The bolts at this flange splice plate were drawn up tight, and welds were in place during one set of vibration tests and the bolts were removed and welds cut off during another set. Consequently, the tests were performed for two different structures; one set was with effective outrigger braces and the other was with the braces removed. The braces were added to the design when the computer optimization process made it evident that a 1.22-Hertz constraint goal for minimum natural frequency was almost unachievable because of a separate requirement for a narrow-leg cross section to reduce microwave blocking. The configuration with braces removed was tested to confirm that the frequency without braces was too low and that the braces, which tend to be both physical and esthetic nuisances, were really required.

APERTURE BLOCKING SHADOW AND QUADRIPOD LEG PROFILE

The aperture blocking of the quadripod assembly consists of two types: plane wave and spherical wave. The plane wave is less important and it consists of the areas masked by the subreflector and the area determined by the projection of the legs on the aperture plane. The spherical wave area is much larger, beginning with a width equal to the leg width at the base of the leg and widening as rays from the focal point intersect the leg above the base and then fan out to reach the surface at points beyond the base.

The sketch of the leg cross-section trapezoids for the prior 64-meter antenna and the new 70-meter extension shows a much smaller profile for the 70-meter antenna. Consequently, the blocking effect of the 70-meter quadripod is 3.4% of the aperture; this provides a significant performance advantage with respect to the 6.3% shadow of the 64-meter quadripod. Nevertheless, and notwithstanding confirming analyses by the NASTRAN program, which was also used for buckling analyses, it was thought advisable to field-test the design predictions because of the unprecedented slim-leg profile.

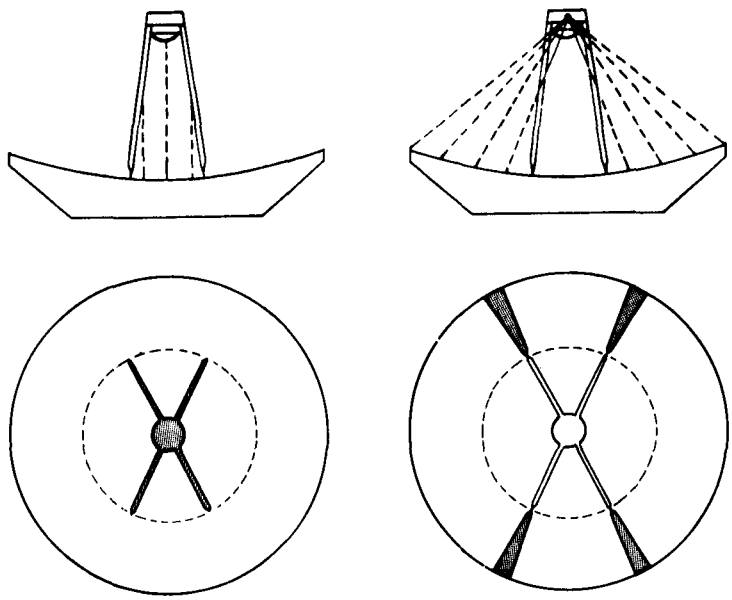

PLANE WAVE AND SPHERICAL WAVE BLOCKAGE

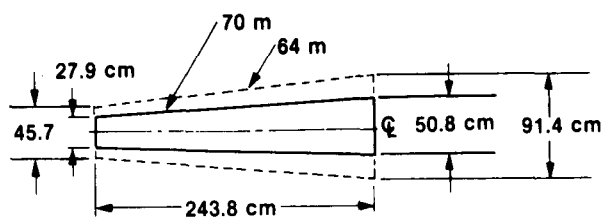

QUADRIPOD CROSS-SECTIONAL PROFILE

ACCELEROMETER AND SHAKER PLACEMENT

The vibration tests were conducted by Kinemetric, Inc., (ref. 10) of California. Ambient tests were first performed to locate the frequencies and characteristics of the lowest modes. This information was used to guide steady-state shaker-excited vibration sweeps that provided confirming information on frequencies, mode shapes, and damping ratios.

The figure shows the accelerometer and shaker locations used during the tests. The Y coordinate on the figure is in the antenna pitch direction, the X coordinate is in the side direction, and the Z coordinate is in the focal direction. Rotations about the Z axis when the antenna points to zenith and about the Y axis when the antenna points to the horizon directly couple with the servo azimuth drive system. At other elevations, components of these motions couple with the azimuth drive. Motions about the X axis can couple with the elevation drive at every antenna attitude.

The eight accelerometer stations A through H indicate possible locations for the instrumentation. Depending upon the particular test and mode shape anticipated from the finite-element model, accelerometers were oriented and reoriented along appropriate axes for each of the tests.

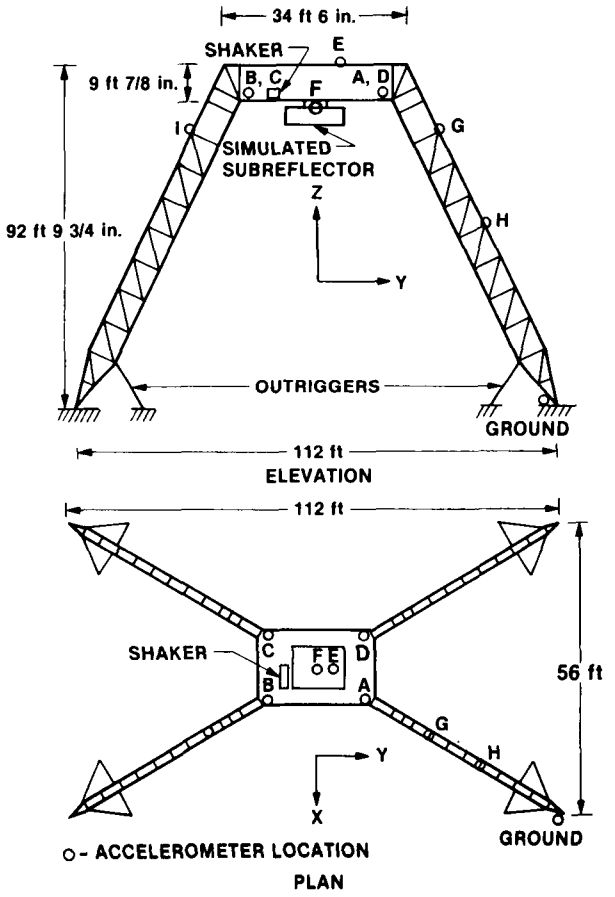

TABULATIONS OF PREDICTED AND MEASURED FREQUENCIES

In addition to observing that the prediction models provide a reasonable representation of the measured frequencies, it can be seen that there really are two different structures (e.g., one without and one with outriggers) with significantly different frequencies. Consistent with the computer design, the outriggers are essential to achieving the 1.22-Hertz constraint.

Measured damping in most cases was less than 1%. The actual damping when on the antenna is likely to be less than measured because several connections that were bolted for the temporary assembly are fully welded at final assembly.

When comparing predictions with measurements, the idealizations made to expedite generating and processing the computer model are of two opposing types:

(1) The model is pin-jointed with 3 degrees of freedom per node. Almost all of the actual joints are fully shop or field welded. This would cause the structure to be stiffer than modeled.

(2) The elastic axes of all members are assumed to meet exactly at the nodal points in the model. The actual detailing and fabrication introduces some small eccentricities at the joints. This would cause the structure to be more compliant than modeled.

NO OUTRIGGER BRACES				WITH OUTRIGGER BRACES			
COMPUTER MODEL		MEASURED		COMPUTER MODEL		MEASURED	
Hz	DESCRIPTION	Hz	DESCRIPTION	Hz	DESCRIPTION	Hz	DESCRIPTION
0.64	TORSION	0.70	TORSION	1.30	TORSION	1.27	TORSION
1.29	X-TRANSLATION	1.36	X-TRANSLATION	1.97	X-TRANSLATION	1.76	X-TRANSLATION
1.55	LEG BENDING	1.74	LEG BENDING	2.72	Y AND PITCH	2.62	Y-TRANSLATION
1.73	LEG BENDING	1.89	LEG BENDING	3.01	LEG TWIST	3.14	LEG BENDING
1.84	LEG TWIST	2.00	LEG BENDING AND TORSION	3.09	LOCAL LEG TWIST	3.38	LEG BENDING
1.96	LEG TWIST	2.14	LEG BENDING AND TORSION	3.25	Y AND PITCH	3.59	LEG BENDING
2.14	LEG BENDING	2.26	LEG BENDING	3.56	Y		
2.15	LEG BENDING			3.79	LOCAL TWIST		
2.21	LEG, LOCAL			4.17	LEG BENDING	4.22	LEG BENDING
2.69	CANTILEVER PITCH	2.48	FIRST Y-TRANSLATION	4.24	LEG BENDING	4.60	LEG BENDING

MODE SHAPE, ELEVATION VIEW

In addition to comparing predicted with measured frequencies, a more stringent test would be to compare mode shapes. To do this, it is necessary to deal with the independent normalizations of the predicted and measured eigenvectors. Here, for each test, the set of mode shapes derived from accelerometer measurements was normalized to the largest component in the set. The corresponding subset of the prediction model eigenvectors was similarly and independently normalized to its own largest component. Consequently, measured and predicted mode shape displacements can be compared on the basis of both direction and, to some extent, magnitude.

The figures show first-mode eigenvector comparisons plotted to an enlarged scale on an elevation view of the quadripod. These are projections on the X-Z plane of the X-axis displacement components.

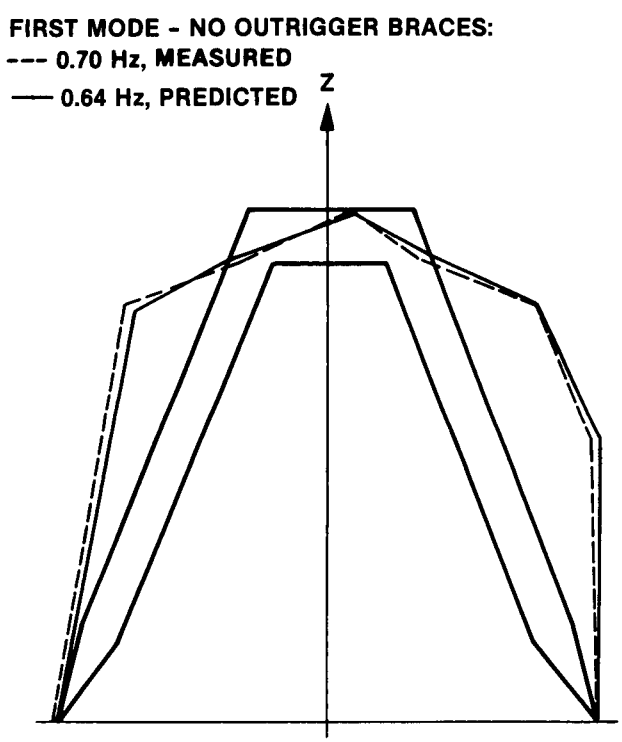

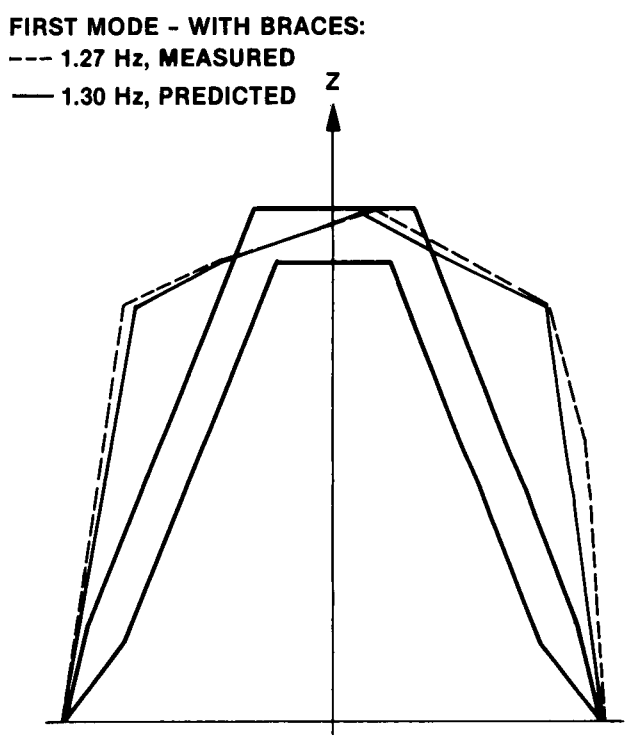

FIRST-MODE EIGENVECTOR COMPARISONS

The Z-axis eigenvector displacement components are usually insignificant in comparison to the X or Y components. Consequently, plotting mode-shape vectors as projected on the X-Y plane provides an almost complete picture of the vector. Notice that here the directions of prediction and measurement vector components are within a few degrees of coincidence and the magnitudes tend to agree also.

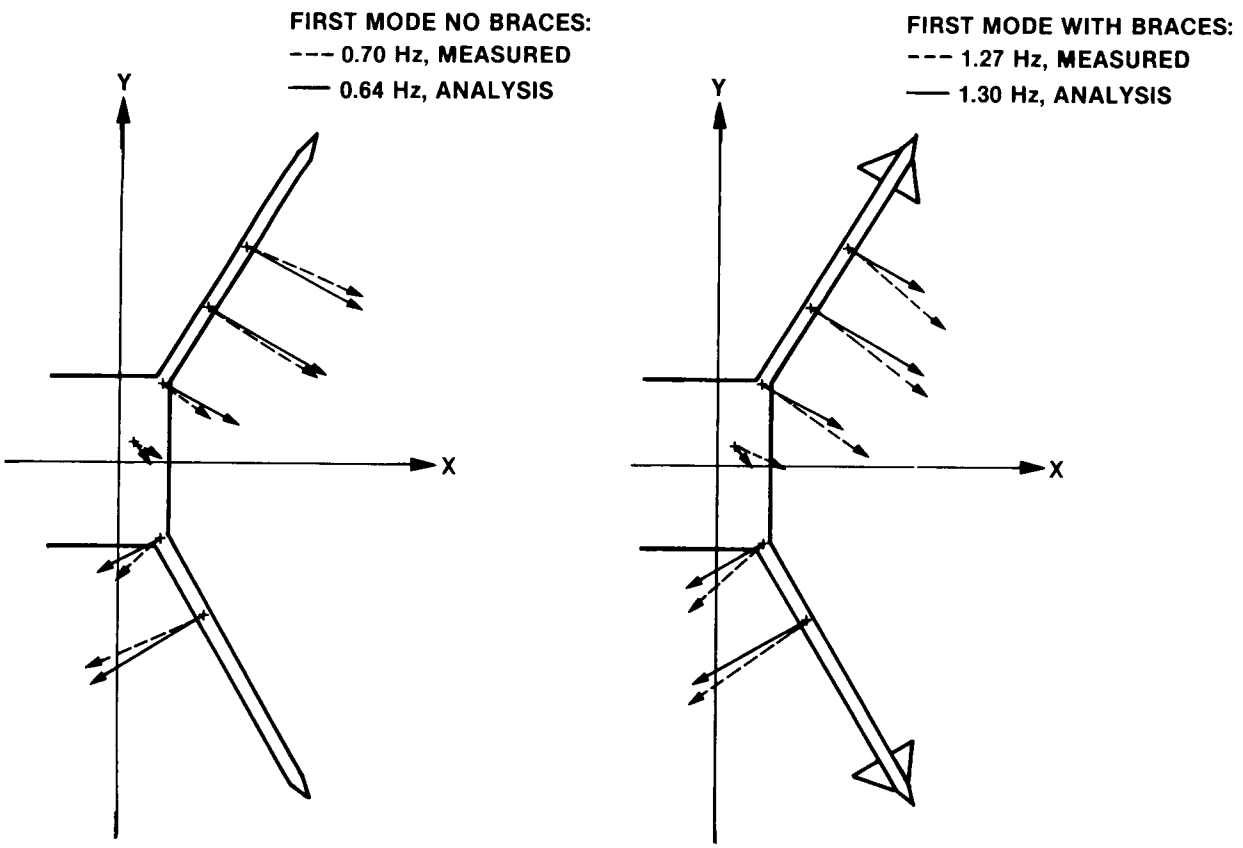

SECOND-MODE EIGENVECTOR COMPARISONS

The correspondence between second-mode predicted and measured eigenvectors is seen to be about as consistent in direction and magnitude as for the first mode.

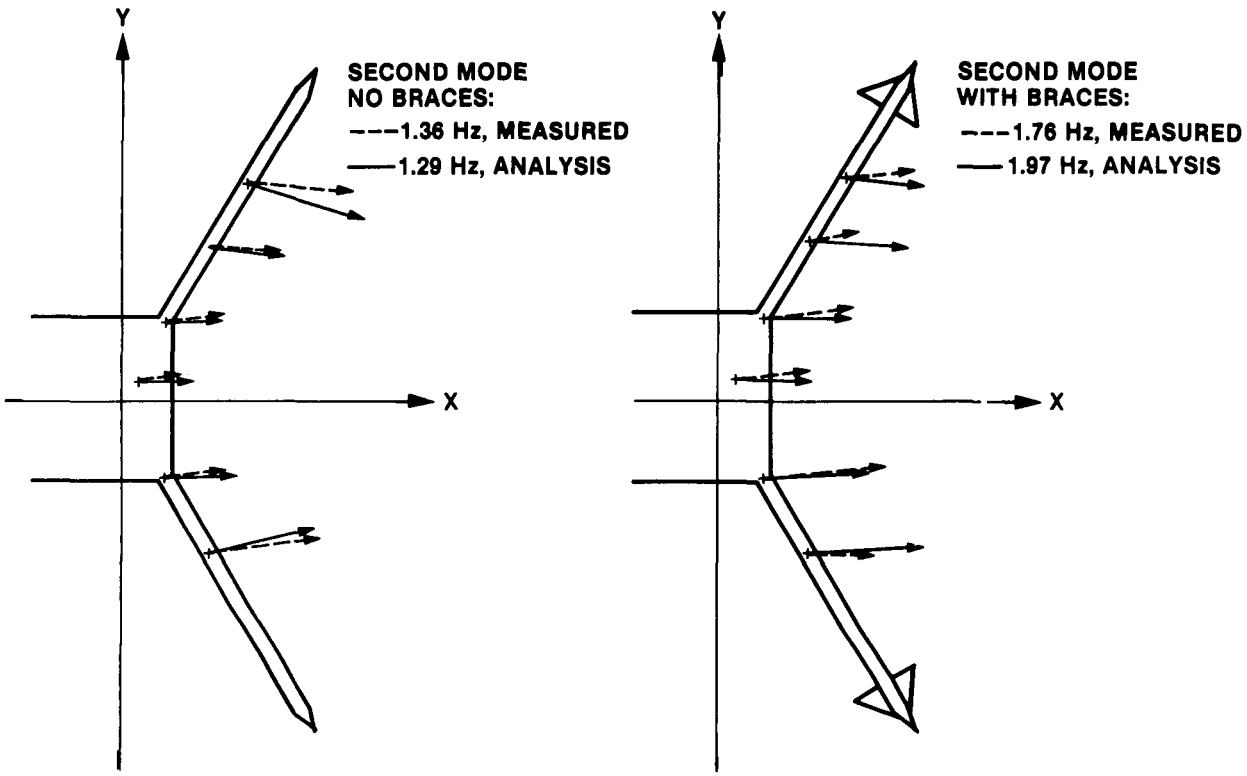

70-METER STRUCTURE

This is the assembled 70-meter structure with quadripod in place. The picture was taken from an erection crane prior to installation of the surface panels. The panels were installed subsequently with a precise ranging theodolite used to set target points on the panels to prescribed coordinates. The setting was done for convenience at the zenith (90-degree) elevation. Rather than setting the surface to the exact contour, the setting coordinates were adjusted by the computer model predictions of the changes from the 45-degree optimum "rigging" angle. Since the validity of biased panel setting depends upon the accuracy of the computer model prediction, and since there were questions about the achieved surface accuracy after the antenna went into operation, two types of field tests were performed. For one type, the antenna remained at the zenith elevation and a 10,000-pound load was applied at specific points of the structure; the change in theodolite reading under load was compared with model predictions. The second type consisted of theodolite measurements of differences in displacements of selected nodes of the structure at the zenith and 45-degree elevations. The changes in measurements at these two elevations were then compared with predictions from the model.

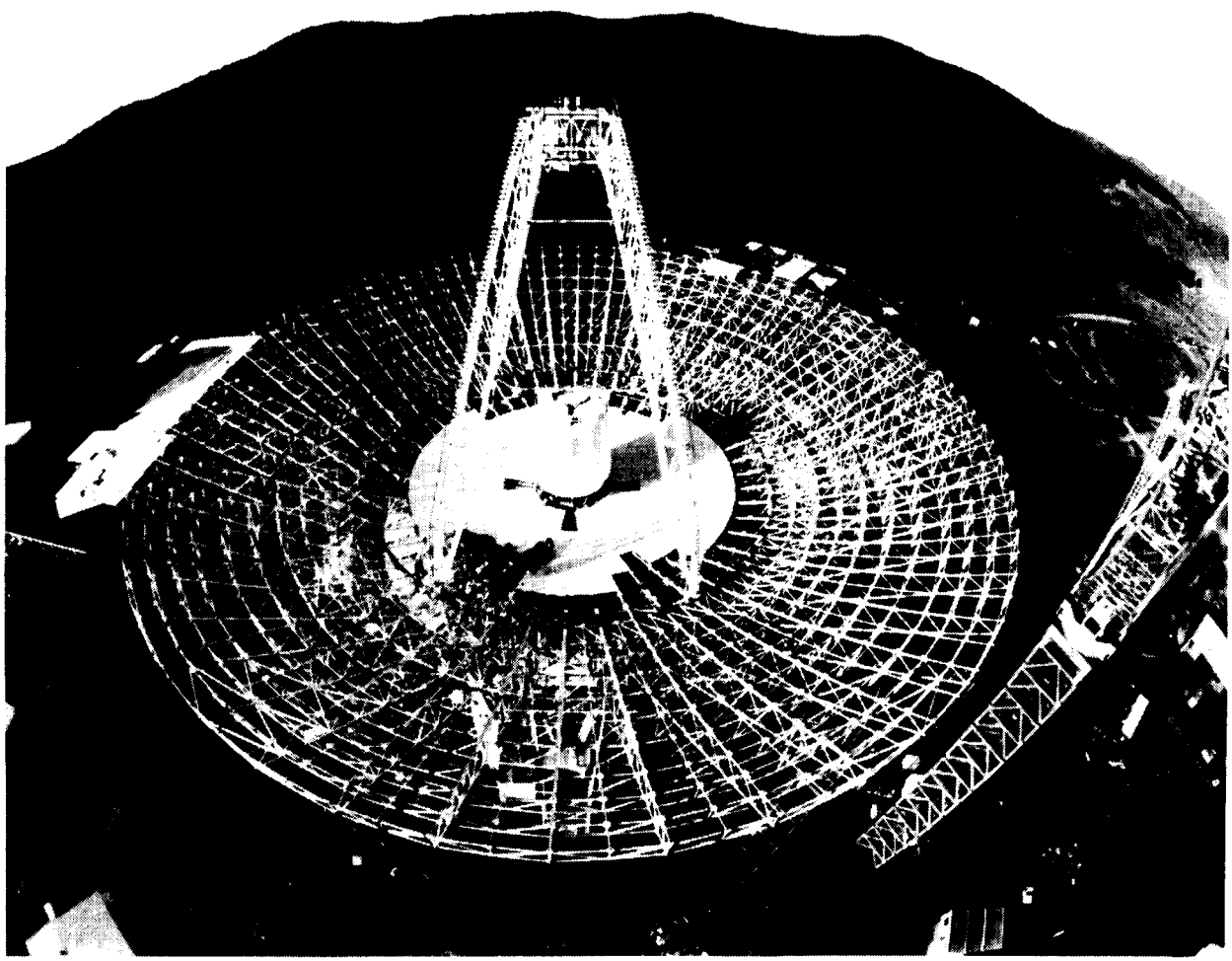

10,000-POUND PULL-TEST SETUP

The loads were all applied at the zenith elevation. One 10,000-pound load was applied in each test. The figure shows two application points and two load directions at each point. There were three candidate ribs for loading: the north rib (rib 1), the east rib (rib 25), and one other rib, called the "northeast rib" (rib 17) at 60 degrees from the north rib. Not all possible tests were completed. In particular, the B2 tests were abandoned because the deflections were too small for reliable measurements. Nevertheless, 12 load tests were completed; 6 before the panels were placed and 6 after. The panels are idealized in the computer model as parasitic, and the actual connections to the trusses are designed to avoid a load path through the panels. Unfortunately, there were not enough matching cases to determine if the panel effect on the deflections was significant. The limited information available indicates that any panel effect is of secondary order.

Several sets of theodolite reading repetitions were completed for a group of targets dispersed over the surface. Each target was read six times in each set of readings. It was determined that the standard error of theodolite reading repeatability was about 0.6 milligrads (2.5 arc seconds) and the error did not appear to be affected by the range to the target.

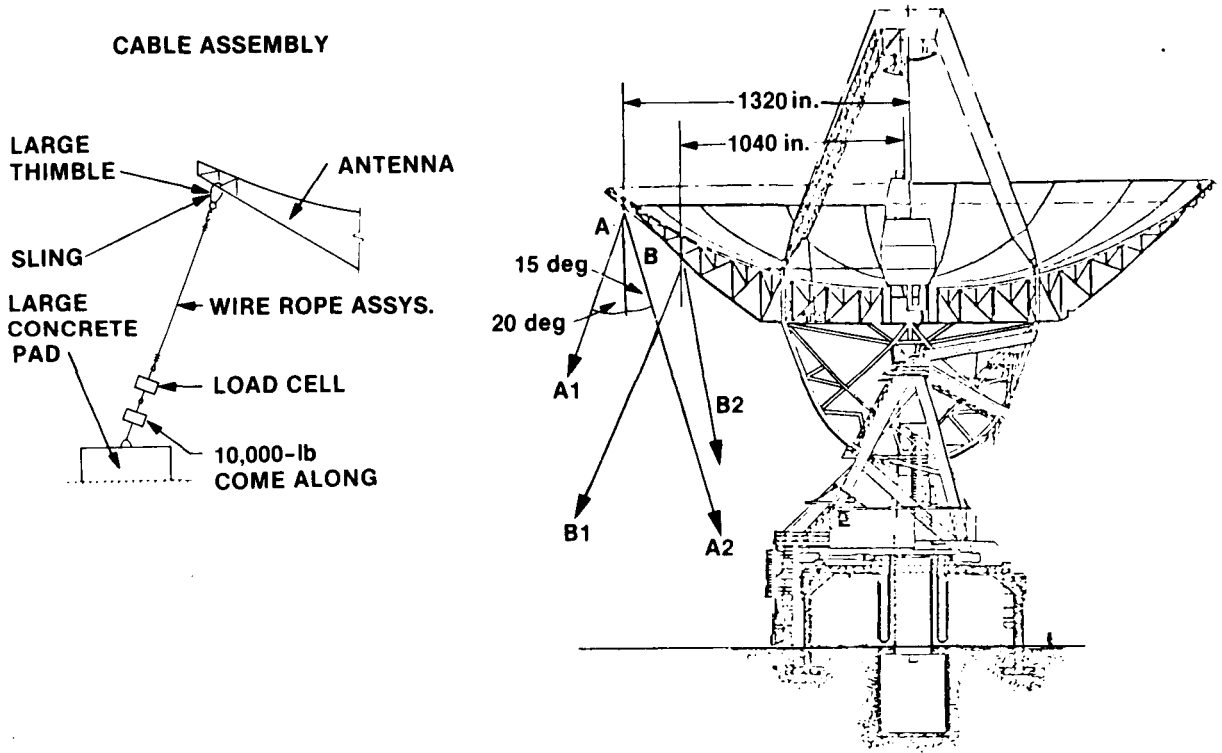

TEST LOAD ON NORTH RIB

The line-of-sight (LOS) offset is computed as the change in theodolite angle times the slant distance to the target point. This is test A1N (the A1 load of figure 15 on rib 1). The curves in the top plot contain points on the loaded rib. The curves in the bottom plot are the offsets for points on the outermost ring. The ribs are numbered 1 at the north, 25 at the east, 48 at the south, and -25 at the west. Any negative rib number is in the western half, and rib -47 is adjacent to rib 48.

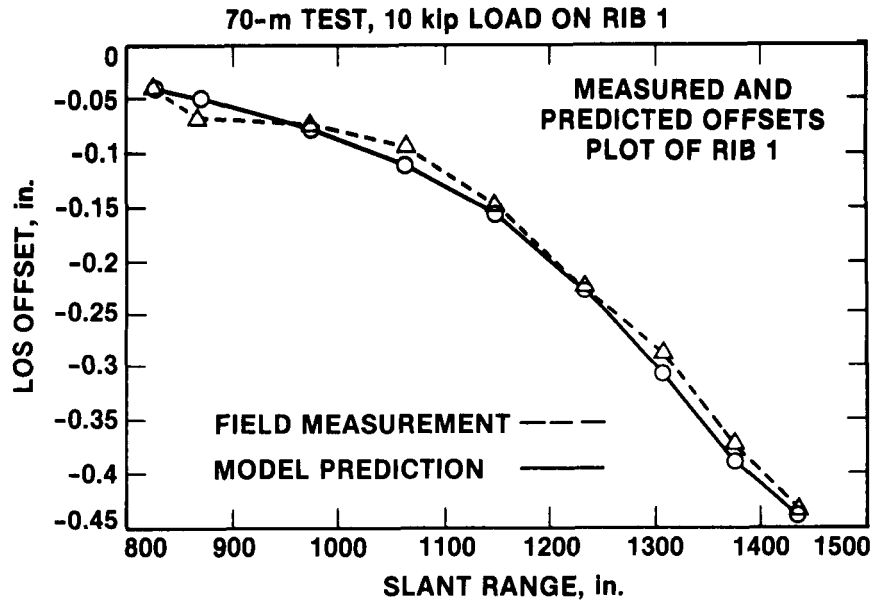

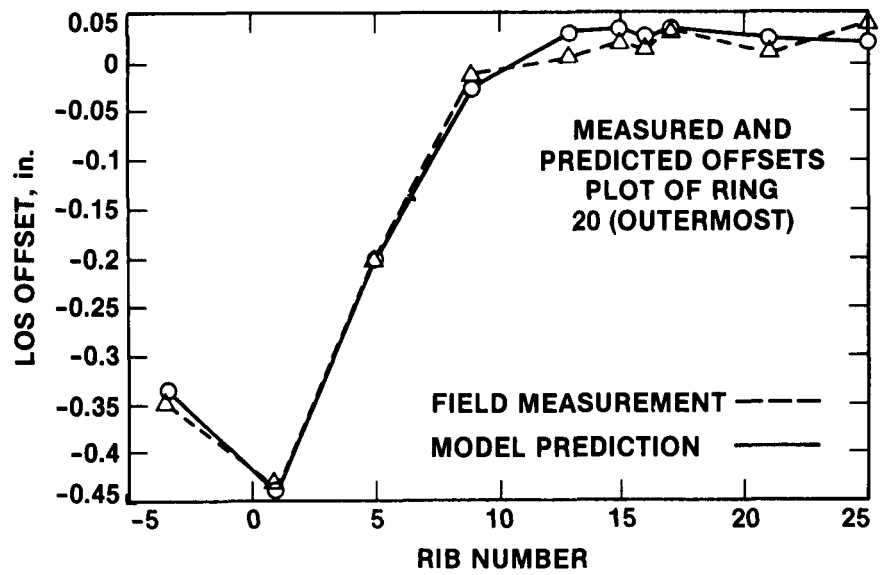

NORTH-RIB LOADING STATISTICAL ANALYSIS

One hypothesis that could be tested is that the model predictions and measurements agree, and the observed differences are due to the measurement error of the theodolite reading. Fortunately, we have a substantial amount of data on theodolite reading repeatability and therefore have a good idea of this standard deviation. Then, if we assume the reading errors have the normal distribution, we can compute the percentile bands of the expected differences between measurement and prediction.

In the top plot, the predictions are plotted on one axis and the measurement at the same point on the other. The units of plotting are in milligrads (1 grad = 0.9 degrees) of angle change. If there is perfect agreement, all points would fall on the 45-degree sloped line through the origin. On the other hand, since we do not expect perfect agreement because of theodolite reading variations, we should expect, for example, that about half the points would fall within the 50% confidence band (0.675 standard deviations) and not more than about 10% would fall outside of the 90% confidence band (1.675 standard deviations). The residual differences are shown on the bottom plot, and here, because of the scale, the confidence bands can be seen more clearly. The mode labels are equal to 100 times the rib number plus a two-digit ring identification. Of the 30 points plotted, 11 fall within the 50th percentile and 2 fall beyond the 90th percentile.

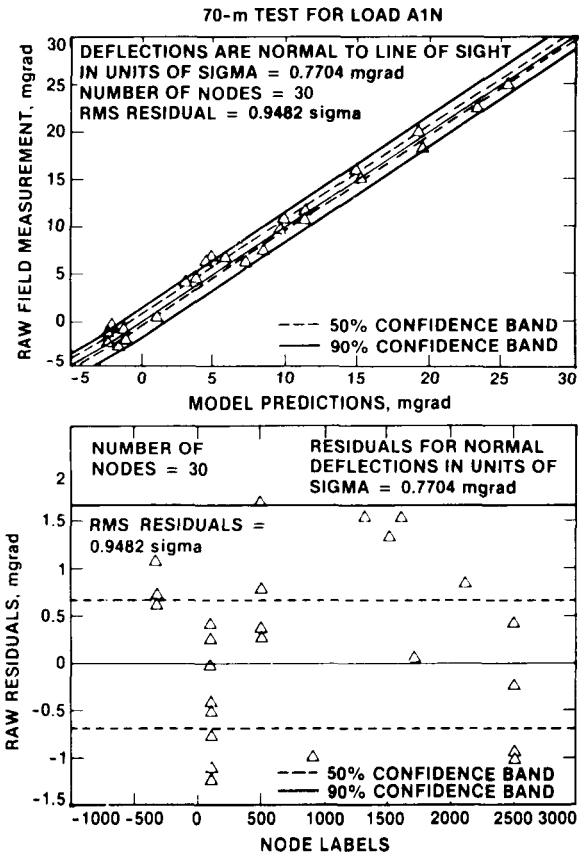

TEST LOADS ON EAST AND NORTHEAST RIBS

The agreement shown between measurements and predictions for these two loading cases and the previous cases (preceding figure), which are all Al type of pull loads, is representative of the full set of loading tests. The statistics and within-band counts for the two cases shown here would also be similar to those of the preceding figure.

A conclusion of the statistical evaluation of all of the processed data from the 12 loading cases is that the measurements agree with the predictions within reason. The differences at the points of maximum deflections are within 5% of the deflection. Of the variability between measurement and model, about 65% of the variance is measurement error and the remaining 35% is attributed to modeling error. Consequently, at the points of maximum deflections, the error in the model is not more than about 3%.

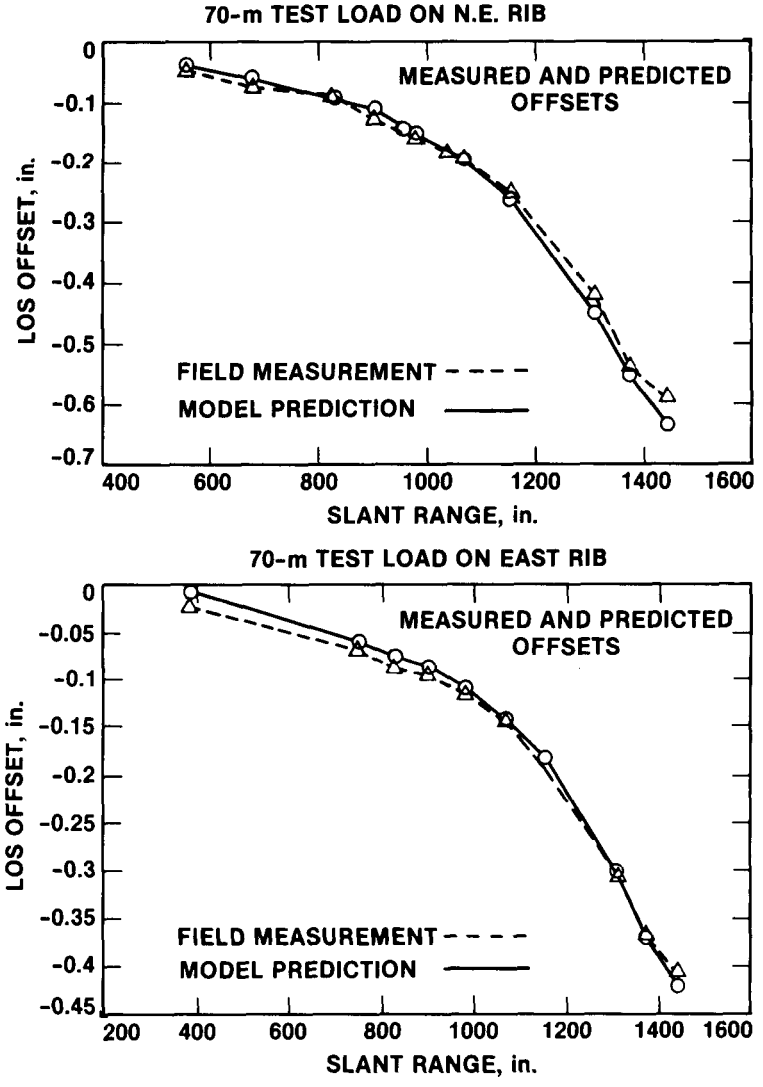

MAIN-RIB GRAVITY LOADING DIFFERENCES IN OFFSETS

The data here is obtained from theodolite measurements at 45-degree and zenith (or near zenith) theodolite measurements. The previously described pull loading tests were limited to a 10,000-pound change in load. Here the effect of the change in gravity loading is much larger and the deflections are from two to three times as large. Consequently, the theodolite repeatability errors are less significant and in many cases are much less than differences in measurement and model.

The loading that produces these offsets is due to the change in orientation of the gravity vector from the 88.5- to 45-degree elevations. One graph gives the offset in millidegrees of theodolite reading and the other graph converts the angle offset to linear projections from the theodolite line of sight. The two graphs give a different perspective of the differences between predictions and measurements. For example, the linear graph weights comparisons by the distance to the point and appears to smooth the angle graph. The linear graph is of most interest in considering differences in microwave path length from the ideal surface. The best fitting here applies to a rigid-body adjustment of the orientation of the field-measurement theodolite. This is necessary because in changing elevations we had no record of the changes in the displacements of the theodolite mounting point.

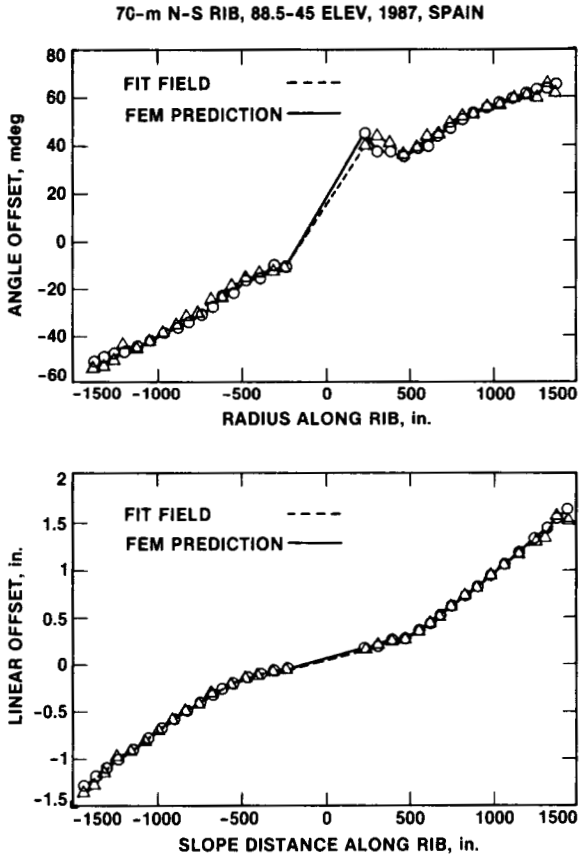

OUTER-RING GRAVITY LOADING DIFFERENCES IN OFFSETS

In addition to theodolite measurements of the main-rib offsets, another set of 90- and 45-degree elevation readings were taken at the two outermost rings (21 and 20) for a 360-degree dispersion of the ribs. Again, rib numbers 1 and 48 are at the north and south tips of the main rib of the preceding figure. The rib-20 plots have been lowered by 20 milligrads for clarity.

Here, and also on the previous curves, measurements and predictions appear to track each other well. The maximum differences between measurements and predictions are not more than about 1/8 inch and typically are much less than this. Nevertheless, as small as the discrepancies might appear here, they are larger than desirable for accurate prediction of microwave performance. The previously discussed set of 10,000-pound applied loading tests was undertaken in the attempt to obtain information to improve the model.

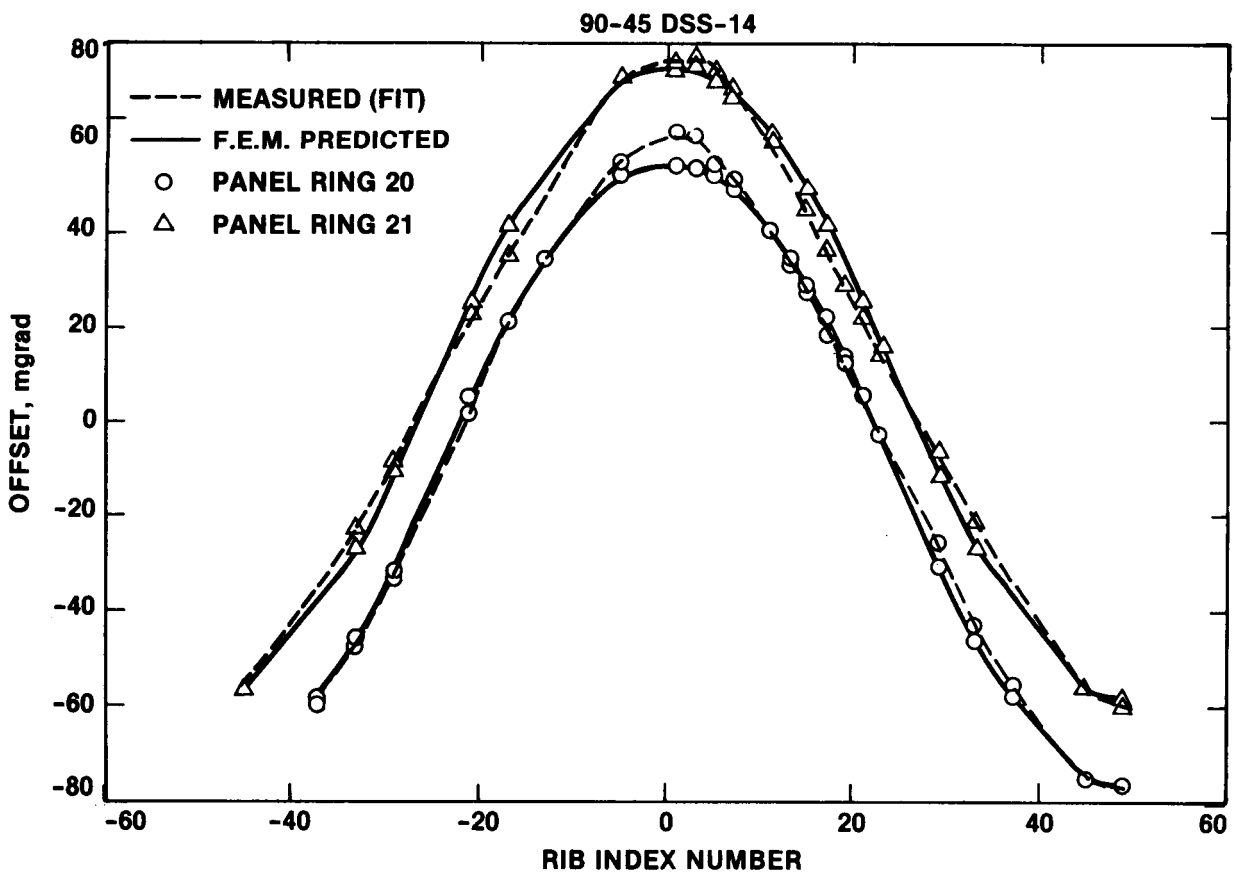

CONCLUSIONS

Considering that the quadripod computer model had known simplifying idealizations, the agreement of measurements with predictions was closer than both needed and expected.

There are some remaining puzzles in the reflector model. The models definitely capture the gross deflected shape but do not agree with the measurements to within current-day microwave frequency requirements for accuracy. Beyond the information presented here, a number of hypotheses have been proposed and tested as possible explanations. Some of these cover simplifying idealizations within the model and others cover model discrepancies. So far, none have been able to provide a satisfactory explanation. Our work is continuing and we look forward to obtaining microwave holography data shortly. This data will give us a complete map of the surface deformations at several different elevations and a much more complete picture than currently available through the limited number of theodolite measurements.

- **QUADRIPOD**
  - **MEASURED FREQUENCIES AND MODE SHAPES CONFIRM THE MODEL PREDICTIONS.**
  - **THE OUTRIGGERS ARE NECESSARY TO ACHIEVE THE REQUIRED MINIMUM NATURAL FREQUENCY.**
- **MAIN REFLECTOR**
  - **THE 10,000-lb LOAD TESTS SUPPORT THE HYPOTHESIS THAT THE MODEL REPRESENTS THE STRUCTURE.**
  - **THE CHANGE IN ELEVATION MEASUREMENTS INDICATE THAT THE MODEL REPRESENTS THE MEASURED GROSS DEFLECTION PATTERNS WITHIN REASON.**
  - **NOTWITHSTANDING THE GOOD REPRESENTATION OF GROSS DEFLECTIONS, THE RESIDUAL DEFLECTIONS ARE LARGER THAN DESIRABLE.**
- **CONCLUSION**
  - **FURTHER STUDY, AND POSSIBLY MORE DATA, MAY BE NEEDED TO EXPLAIN THE RESIDUAL ERRORS.**

REFERENCES

1. Utku, S., and Barondess, S. M. , Computation of Weighted Root-Mean-Square of Path Length Changes Caused by the Deformation and Imperfections of Rotational Paraboloidal Antennas. Technical Memorandum 33-118, Jet Propulsion Laboratory, Pasadena, California, March 1963.

2. Levy, R., Computer Design of Antenna Reflectors. AIAA/ASME/SAE, 14th SDM Conference, Paper 73-351, Williamsburg, Virginia, March 20-22, 1973.

3. Levy, R., and Melosh, R. J., Computer Design of Antenna Reflectors. Journal of the Structural Division, Proc. ASCE 99 (ST-11), Proc. Paper 10178, pp. 2269-2285, November 1973.

4. Schmit, L. A., and Fleury, C., Structural Synthesis by Combining Approximation Concepts and Dual Methods. AIAA Journal, Vol. 18, No. 10, pp. 1251-1260.

5. Levy, R., Optimization of Antenna Structure Design. Eighth Conference on Electronic Computation, ASCE, Houston, Texas, pp. 114-129, February 21, 1983.

6. Levy, R., and Parzynski, W., Optimality Criteria Solution Strategies in Multiple Constraint Design Optimization. AIAA Journal, Vol. 20, No. 5, pp. 708-715.

7. Levy, R., and Chai, K., Implementation of Natural Frequency Analysis and Optimality Criterion Design. Computers and Structures. Vol. 10, 1979, pp. 277-282.

8. Kamat, M. P., Venkayya, V., and Khot, N., Optimization with Frequency Constraints - Limitations. Journal of Sound and Vibration. 1983, Vol. 91, No. 1, pp. 147-154.

9. Grandhi, R., and Venkayya, V., Structural Optimization with Frequency Constraints. AIAA/ASME/ASCE/AHS, 28th SDM Conference, Paper 87-0787-CP, Monterey, California, April 6-8, 1987.

10. Vibration Measurements of Quadripod and Apex Structure for 70M Antenna, DSS-63. Kinemetric, Inc., 222 Vista Avenue, Pasadena, California, 91107, May 2, 1986.